Research Square

Preprints are preliminary reports that have not undergone peer review.
They should not be considered conclusive, used to inform clinical practice,
or referenced by the media as validated information.

Designing d-π•••π-d Conductive Networks in Molecular Cluster Crystals via Precise Rare-Earth-Directed Assembly

Wei-Hui Fang

fwh@fjirsm.ac.cn

Fujian Institute of Research on the Structure of Matter, Chinese Academy of Sciences
https://orcid.org/0000-0003-3358-3057

Zhihao Lu

Fujian Institute of Research on the Structure of Matter, Chinese Academy of Sciences

Qingshun Fan

State Key Laboratory of Structural Chemistry, Fujian Institute of Research on the Structure of Matter

Song Lin

State Key Laboratory of Structural Chemistry, Fujian Institute of Research on the Structure of Matter

Cuiming Ren

State Key Laboratory of Structural Chemistry, Fujian Institute of Research on the Structure of Matter

Changdong Liu

State Key Laboratory of Structural Chemistry, Fujian Institute of Research on the Structure of Matter

Mingbu Luo

State Key Laboratory of Structural Chemistry, Fujian Institute of Research on the Structure of Matter

Lehua Zhang

School of Resources and Environmental Engineering, East China University of Science and Technology

Li Xu

State Key Laboratory of Structural Chemistry, Fujian Institute of Research on the Structure of Matter

Article

Keywords:

Posted Date: February 25th, 2026

DOI: https://doi.org/10.21203/rs.3.rs-8669464/v1

License: This work is licensed under a Creative Commons Attribution 4.0 International License.
Read Full License

Additional Declarations: There is **NO** Competing Interest.

Version of Record: A version of this preprint was published at Nature Synthesis on August 26th, 2026. See the published version at https://doi.org/10.1038/s44160-026-01138-w.

Abstract

Molecular-based crystalline conductors, with their highly ordered structures, are highly valuable for clarifying how molecular arrangements determine electronic properties. However, conventional zero-dimensional cluster materials generally exhibit low conductivity due to the difficulty in establishing efficient conductive networks within their isolated systems. In this study, we constructed an electron-rich dimeric molecular conductor by introducing the aromatic metal-cluster building block {MoIV3py3} as a stereogenic unit while encapsulating rare-earth ions. This design enables the formation of a novel d-π•••π-d conjugated conductive pathway between otherwise isolated clusters. Among the systems, the hexagonal phases embedded with Sm and Eu ions exhibit the shortest π•••π contact distance (3.65 Å) and possess the highest in-plane (ab-axis) conductivity of 3.17 × 10^{-5} S•m^{-}1 and 2.94 × 10^{-5} S•m^{-}1, respectively—more than 105 times higher than that of conventional polyoxometalates. The incorporation of rare-earth ions not only induces the formation of a semiconducting hexagonal phase and a metallic-like tetragonal phase but also enables the modulation of anisotropic charge transport in single crystals. This work provides an important design strategy and synthetic pathway for the tailored construction of cluster-based crystalline materials with targeted electrical properties.

Introduction

Crystalline molecular conductors, due to their well-defined molecular structures, are of great importance in elucidating the relationship between structural characteristics and the electronic properties of materials, and in uncovering novel physical phenomena[1,2]. Currently, leading crystalline conductive materials rely on the continuous linkage forming conductive pathways[3,4]. However, isolated cluster materials have remained underexplored in the field of electrical conductivity. This is primarily because the inherent challenge of establishing an effective conductive network in such discrete systems leads to insulating behavior, thus rendering them less attractive for electronic applications. Therefore, developing conductive materials from discrete clusters presents a compelling direction[5,6].

Polyoxometalates (POMs) are a typical example of clusters, and as electron reservoirs, they have garnered significant attention due to their unprecedented versatility in terms of shapes, large sizes, molecular/electronic structures and bonding, as well as unique physicochemical properties[7]. Nonetheless, analogous to the poor conductivity observed in most metal-organic frameworks (MOFs), POMs are widely considered electrical insulators, which significantly restricts their applications in POM-based nanoelectronics (POMtronics)[8,9]. The primary reason is that conventional polyoxometalates are fully oxidized d^0-systems: their periphery is occupied by inert M=O double bonds[10], which prevents effective connection with organic ligands to form $d–\pi$ conjugation and, consequently, limits the construction of electron-transport networks[11]. A common strategy is to introduce organic molecular conductors and form POM-containing radical salts, such as TTF-based POM materials[12]. This conduction mode predominantly depends on the highly conductive organic ionic component to form an electron-transport pathway (ETp)[13]. However, this strategy does not actually rely on the intrinsic

conductivity of the POM clusters, thus failing to the full exploitation of their unique electronic structure. The one-dimensional (1D) stacking of these organic ions[14] further induces pronounced anisotropy in conductivity ($a_a \ll c_c$)[15,16]. In addition, although rare-earth elements are widely exploited in magnetism, optics, catalysis, and energy, their potential for tuning the electrical conductivity of crystalline materials remains largely unexplored.

Herein, unlike the conventional strategy of constructing radical salts, we enhanced the intrinsic conductivity of the POM clusters and, by establishing a distinctive *d*–*π*···*π*–*d* networks between the clusters and organic ligands. By exploiting *π*···*π* conjugation between the aromatic rings at the two ends of the linear dimeric cluster, we realized *d*–*π*···*π*–*d* 3D conductive frameworks jointly constructed by the organic ligands and the clusters. Moreover, the tunable anisotropy of electrical conductivity arises from the Ln^{2+}/Ln^{3+} redox shuttle along the *c*-axis and *π*···*π* interactions along the *a*-axis, both governed by the endohedral Ln^{3+} dimers, which also exert significant influence on the electronic structure. It represents a significant advance for constructing robust cluster-based conductive networks that fully exploit the unique electronic structure of polyoxometalate clusters. Moreover, the anisotropy of electrical conductivity can be tuned by the Ln^{2+}/Ln^{3+} redox shuttle along the *c* axis and *π*···*π* interactions along the *a*-axis, both of which are modulated by the endohedral Ln^{3+} dimers and their influence on the electronic structures.

Scheme 1 Design innovation of crystalline molecular-cluster conductive networks: A comparative illustration between conventional systems and the present work. Left: Typical molecular-cluster crystals exhibit only 1D π···π interactions (σ_c: 1D interactions), lack effective electronic transfer pathways (ETp; σ_a: no ETp), and display charge transport limited by the packing of counterions and clusters. Right: In this work, a *d*-*π*···*π*-*d* conductive network was constructed, achieving three key advancements—enhanced conductivity, tailorable electrical anisotropy (σ_a/σ_c), and tunable semiconductor-to-conductor switching. Through the synergistic assembly of quasi-aromatic metal clusters, *π*-aromatic rings, and Ln dimeric belt motifs, forming through-space *d*-*π*···*π*-*d* charge transport channels. Coupled with Mo^{IV}/Mo^{VI} and Ln^{II}/Ln^{III} redox shuttles, this network facilitates *d*-*π*···*π*-*d* transport along the *ab* direction (σ_{ab}) and redox-mediated conduction along the *c* direction (σ_c), thereby overcoming the charge-transport limitations of conventional systems.

Results and Discussion

Self-assembly of quasi-aromatic clusters

The coordination geometry of building blocks is one of the important parameters in controlling the dimensionality of resulting framework structure[17,18]. The metallic crown-like $\{Mo^{IV}_3\text{-}py_3\}$, with the *π*-aromatics perpendicularly coordinated to the triangular plane of metal–metal bonded Mo^{IV}_3, will be an opportunity to make interconnections in multi-directions. Such quasi-aromatic building blocks were

formed via precursor $[Mo^{IV}_3O_2(O_2CCH_3)_6(H_2O)_3]^{2+}$ in the mixture of pyridine and water under solvothermal conditions[19]. Moreover, the triangular $\{Mo^{IV}_3\text{-}py_3\}$ units, which are intrinsically $d–\pi$ conjugated and storing six electrons, exhibit both π- and quasi-aromaticity[20,21]. They are expected to modulate the electronic structure of the POM cluster, thereby enhancing its intrinsic conductivity.

In contrast to conventional fully-oxidized POMs with endohedral main group heteroatoms X such as P, Si via strong covalent bonds [22], the *trans* effect exerted by the coordinated aromatic rings (Mo^{IV}-py, 2.2 Å *vs*. Mo^{VI}=O, 1.7 Å) markedly strengthens Mo^{IV}_3-μ_3-O bonding (Mo^{IV}_3-μ_3-O, 2.0 Å *vs*. Mo^{VI}_3-μ_3-O, 2.3 Å) and eludes Mo^{IV}_3-μ_3-O-X covalent bonding[23-25]. Nevertheless, the Mo^{IV}_3–μ_3-O can engage in weak coordination bond with central Ln^{III} ions. The clusters are archetypal dimers, assembled by capping both ends of the redox-active $\{Ln_2P_9Mo^{VI}_6\}$ belt with a quasi-aromatic $\{Mo^{IV}_3\text{-}py_3\}$ unit. This structure establishes an intramolecular conductive pathway and endows the clusters with molecular conductor properties. The crystalline phases were selectively tuned via partially oxidative aggregation with H_3PO_3 and $LnCl_3$, yielding a hexagonal phase for La–Gd (Fig. S1, left) and a tetragonal phase for Sm–Tb (Fig. S1, right). Both phases are constructed from metal clusters of the same general formula of $[Ln_2@Mo^{IV}_6Mo^{VI}_6(PO_4)_2(HPO_3)_7O_{26}py_6]^{6-}$ with C_{3h} symmetry in the hexagonal phase (Fig. 1a and Fig. S1, left; Supplementary Video 1) and C_s symmetry in the tetragonal phase (Fig. 1f and S1, right; Supplementary Video 2).

The clusters with endohedral 10-coordinated Ln^{III} atoms crystallize into hexagonal phase and those with 9-coordinated Ln^{III} atoms crystallize into tetragonal phase (Scheme 1 and 2). As illustrated in Scheme 2, the longest Ln···Oa distance in **8**–**11** (2.84(2)–2.96(2) Å) is significantly longer than that in **1**–**7** (2.450(12)–2.695(9) Å) because of the reduced coordination number requirement. This elongation breaks the C_{3h} symmetry in the former, and resulting in the lower crystallographic C_s symmetry observed in **8**–**11**, thus significantly differentiate the connectivity mode among the quasi-aromatic $\{Mo^{IV}_3O_4py_3\}$ SBUs via $\pi\cdots\pi$ interactions, and forming hexagonal and tetragonal conjugated Mo^{IV}_3 phases. Interestingly, the sixfold and fourfold symmetry phases are also similarly exits in Mo metallenes[26].

Scheme 2 Synthetic route and photographs of $[Ln_2@Mo^{IV}_6Mo^{VI}_6(PO_4)_2(HPO_3)_7O_{26}py_6]^{6-}$ crystals showing a rare-earth-induced hexagonal-to-tetragonal phase transition. Scale bars, 0.15 mm. Color code: Mo^{IV}, red purple; Ln, olive; P, pale brown; O, red; C, gray. The crystals were directly imaged from the mother liquor without prior isolation or selection.

The chemical bonding states of Mo^{IV} were confirmed by strong triangular $Mo^{IV}(d^2)$-$Mo^{IV}(d^2)$ metal–metal bonds (2.498(3)–2.536(3) Å) and X-ray photoelectron spectroscopy (XPS) (Fig. 2c, 2d and S5, Table S5) that reveals two intense peaks at binding energies of 233.5 and 230.4 eV, corresponding to $3d_{3/2}$ and $3d_{5/2}$ of Mo^{IV}, respectively. Most remarkable is the quasi-aromatic metal–metal bonded $\{Mo^{IV}\text{-}py\}_3d\text{-}\pi\cdots\pi\text{-}d$ conjugated systems (Mo-N, 2.187(16)–2.234(17) Å) interconnected by the strong

triangularly metal–metal bonded Mo^{IV}_3 units, which are essential to constitute long-range electron transport.

2D aromatic {Mo^{IV}_3-py_3} π-stacked layers

Fig. 1. Assembly of *d*-*π*···*π*-*d* conductive networks in molecular-cluster crystals, directed by lanthanide ions, modulated by their coordination environment (geometry, coordination number, and symmetry). (a, f) Coordination environments of the lanthanide ion in the hexagonal phase (10-coordinate, C_{3h} symmetry) and the tetragonal phase (9-coordinate, C_s symmetry), respectively, with Eu–O_a bond lengths labeled (2.45 Å in the hexagonal phase and 2.28 Å in the tetragonal phase). Color shading highlights the structural features of the lanthanide coordination units. (b) Primary structural building units of the hexagonal-phase clusters assembled in an antiparallel-sandwich arrangement. (c) Further assembly into Kagome-type *d*-*π*···*π*-*d* conjugated layers in the hexagonal phase. (d) 3D crystalline network with **acs** topology constructed from the hexagonal phase. (e) Assembly features of the quasi-aromatic {$Mo^{IV}_3O_4$} cluster units in the tetragonal phase, exhibiting a 30° antiparallel displaced and edge-tilted-T *π*···*π* stacking configuration. (g) *d*-*π*···*π*-*d* conjugated layer structure formed in the tetragonal phase. (h) Finally, 3D crystalline network with **cfu** topology constructed from the tetragonal phase. Color code: Mo^{IV}, red purple; Mo^{VI}, teal; Ln, olive; P, pale brown; O, red; C, gray; antiparallel-sandwich stacked py, magenta; edge-tilted-T stacked py, sky blue; mono 30° antiparallel-displaced py, light green; dual 30° antiparallel-displaced py, orange; lattice py, yellow. H atoms are omitted for clarity.

Replacing the terminal $Mo^{V,VI}$=O groups in conventional POM$o^{V,VI}$s by electron-rich Mo^{IV}←py π-conjugated systems in aromatic POMo^{IV}s makes possible to constitute *π*···*π* stacking supramolecular frameworks in POMs, and thereby dramatically enhances their electrical conductivity. The present work confirms that this methodology is feasible, and thus paves a new avenue to make multidimensional electroconductive cluster materials. As shown in Fig. 1b, in the hexagonal phase, each crown-like {Mo^{IV}-py}$_3$ building unit interacts with the surrounding three {Mo^{IV}-py}$_3$*π*-conjugated systems through antiparallel-sandwich py···py *π*-stacking interactions, forming extended Mo^{IV}_3 bilayer in the *ab* plane (Fig. 1c; Supplementary Videos 3 and 5). The *π*···*π* distance ranges from 3.65 Å (**5-Sm** and **6-Eu**) to 3.86 Å (**2-Ce**), and reveals strong *π*···*π* interactions between antiparallel arranged py ligands, which together with the triangular Mo-Mo and Mo-N bonds provide highly efficient 2D ETp networks. While the tetragonal {Mo^{IV}_3-py_3} conjugating layer in **8**–**11**, is composed of antiparallel-displaced py···py and C-H···py (edge-tilted-T) *π*-stacks (Fig. 1b, 1e and Supplementary Videos 4 and 6)[27]. It is noteworthy that the tetragonal symmetric Mo^{IV}_3 conjugating layers showed smaller interlayer distance of ~3.13 nm compared with those of sixfold symmetric Mo^{IV}_3 conjugating layers of 3.23~3.28 nm, indicating intrinsically higher electrical conductivities (Table S4).

Due to the stereo {Mo^{IV}_3-py_3} SBU, the *π*···*π* stacking along *ab*-directions via the three coordinated py rings, rather than 1D *π*-stacking as MOFs, that guided anisotropic growth of conjugated Mo^{IV}_3 layer in 2D

plane that crystallize into plate morphology (Scheme 2). It is well known that 2D graphene analogue materials feature strong in-plane covalent bonds and weak interlayer $\pi\cdots\pi$ interactions. On the contrary, our bilayer Mo^{IV}_3 showed unique in-plane covalent bonds (coordinate and metal–metal bonds) and $\pi\cdots\pi$ interactions, and strong interlayer covalent bonds.

According to the crystal structures, the hexagonal Mo^{IV}_3 clusters possesses **acs** topology (Fig. 1d), while **cfu** topology for the fourfold symmetry phase (Fig. 1h). A sideview of hexagonal phase clearly shows the zig-zag Kagome layers constructed by the six-connected $\{Mo^{IV}_3\text{-}py_3\}_2$ clusters, thus performed a Kagome lattice. As shown by the side of view of the topological nets, the Mo^{IV}-Mo^{IV}/Mo^{IV}-py/Ln^{III}_2@$Mo^{VI}(HP^{III})_7P^{V}_2O_{49}$ bonds and py$\cdots$py π-stacking interactions, contribute to ETp along both *ab* plane and *c*-axis.

Due to the extended $d–\pi\cdots\pi–d$ conjugation along the *ab* plane, these $\{Ln_2(Mo^{IV}_3py_3)_2\}$ clusters preferentially crystallize into hexagonal or tetragonal plate-like morphologies (see Scheme 2 and Fig. S3). TEM provides distinct morphology of conjugated $\{Ln_2(Mo^{IV}_3py_3)_2\}$ clusters. As shown in Fig. 2f, the TEM images of hexagonal **4-Nd** nanosheets similarly showed lattice fringes with the fringe space distance of 1.63 nm on (002) reflection. While for tetragonal **9-Eu,** the TEM images distinctively show the sideview along different directions of the 2D cluster-conjugated layers (Fig. 2i).

Fig. 2 Structural characterization of $\{Ln_2(Mo^{IV}_3py_3)_2\}$ clusters through XRD, XPS, and electron microscopy. (a, b) Experimental and simulated powder X-ray diffraction (PXRD) patterns for $\{Ln_2(Mo^{IV}_3py)_2\}$ clusters in the hexagonal (a) and tetragonal (b) phases, demonstrating phase purity and structural agreement. (c, d) XPS analysis confirming the Mo^{IV} state. (e–j) Field emission transmission electron microscopy (FETEM) images and FFT patterns displaying the crystallinity and lattice structure of the hexagonal (e-g) and tetragonal (h-j) phases.

Enhanced electrical conductivity

Fig. 3. Electrical conductivity characterization of $\{Ln_2(Mo^{IV}_3py_3)_2\}$ materials: (a) Typical *I*–*V* curves showing the single-crystal conductivity of $P6_3/m$ symmetric **1–7** along the *a*-axis, acquired using the two-probe method. (b) Typical *I*–*V* curves showing their conductivity along the *c*-axis. (c) Summary of single-crystal conductivity (*a*- and *c*-axis), HOMO–LUMO gaps, and π-stacking distance of the aromatic clusters. (d, e) Arrhenius representation of the pellet electrical conductivity for hexagonal **6-Eu** (d) and tetragonal **9-Eu** (e), measured via the van der Pauw method.

As illustrated in Fig. 1, the quasi-aromatic $[Mo^{IV}_3O_4py_3]$ incomplete cubane unit can serve as highly stable 6e-redox active units via the reversible cleavage/reformation of the triangular Mo^{IV}–Mo^{IV} bonds. Inspired by the 3D electron transport network of the clusters, the electrical conductivity was measured on grown single crystals by two-probe method at ambient temperature. The electro-conductivity of the crystals was confirmed by measuring the single-crystal conductivity along *a*- and *c*-axis, respectively. As

shown in Fig. 3c, the σ_a values exhibit a strong correlation with the $\pi\cdots\pi$ stacking distance along the *ab* directions. Specifically, **5-Sm** and **6-Eu**, which possess the shortest $\pi\cdots\pi$ distance (3.65 Å), also display the highest σ_a values of 3.17×10^{-5} S·m^{-1} and 2.94×10^{-5} S·m^{-1}, respectively—approximately 10^5-fold higher than those of conventional metal-oxygen clusters (e.g., $TBA_3[PMo_{12}O_{40}]$, $\sigma < 10^{-9}$ S·m^{-1})[28]. Meanwhile, the σ_c values align well with the HOMO–LUMO gaps of the clusters. For instance, **6-Eu**, with the narrowest HOMO–LUMO gap (2.09 eV), exhibits the highest σ_c value of 2.47×10^{-5} S·m^{-1}. The anisotropic ratio of 1.1 (σ_a/σ_c) for single-crystal conductivity of **6-Eu** reveals virtually isotropic electrical conductivities as expected for the 3D electron transport pathways. This is quite different from most conductive MOFs that are characteristic of remarkably anisotropic charge transport[29-31].

The tailorable anisotropic conductivity (σ_a/σ_c) provides a versatile platform for diverse device applications. The crystals with $\sigma_a/\sigma_c > 1$ are optimal for in-plane (2D) electron transport, whereas those with $\sigma_a>\sigma_c$ are advantageous for interlayer transport in vertical devices. For the nearly isotropic conductivity ($\sigma_c \approx \sigma_a$) observed in **6-Eu** renders it suitable for 3D integrated circuits, meanwhile, simplifies device fabrication by eliminating the need for strict crystalline orientation control.

For the hexagonal and tetragonal phases, the temperature-dependent electrical conductivity were studied on their respective Eu species in the temperature range of 250~315 K in pellet samples with van der Pauw method. The conductivity values showed excellent reproducibility during heating and cooling cycles, and **9-Eu**, which has a smaller HOMO-LUMO gap (1.51 eV), exhibits higher electro-conductivity ($\sigma = 1.46\times10^{-6}$ S m^{-1}). Both the hexagonal and tetragonal symmetric phases were confirmed to be semiconducting (Fig. 3d and 3e). The Arrhenius fit to the data revealed an activation energy E_a of just 65 meV for **6-Eu** which is among the smallest E_a reported for semiconducting molecular crystals, MOFs or coordination polymers[32]. While the activation energy of **9-Eu** was 133 meV. The activation energies correspond to the hopping energy barriers based on the nearest neighbor hopping mechanism. The larger intrinsic activation energy of **9-Eu** may be attributed to more variety of π-stacking modes. It is also implied that the comprehensive π-conjugations composed with antiparallel and T-shaped π-stacking aromatics are of a more efficient strategy serving as long range electron transfer, which has been extensively employed by the microbes forming electrically conductive pili to construct a continuous pathway for long-range extracellular electron transport[33,34].

Electronic structures and bonding

The in-plane interactions of hexagonal and tetragonal conjugation of $\{Ln_2(Mo^{IV}{}_3py_3)_2\}$ clusters were confirmed by the independent gradient model (IGM) method to provide a visual understanding of the interactions present in the systems[35]. The van der Waals (vdW) interactions dominated in the conjugated $\{Mo^{IV}\text{-py}\}_3$ layers as the green-colored fields among the clusters (Fig. 4a). While, in addition to the strong $\pi\cdots\pi$ interactions, C-H···O hydrogen bonding interactions (blue clumps) which are stronger in the tetragonal systems, are also of significance in stabilizing the $\{Mo^{IV}\text{-py}\}_3$-conjugated layers (Fig. 4b).

Fig. 4. Colored isosurfaces (isosurface value = 0.006) showing IGM (independent-gradient-model) analysis of multiple Mo^{IV}–π conjugations: (a) the dimer of **6-Eu** under hexagonal symmetry, and (b) the pentamer of **9-Eu** under tetragonal symmetry, in which green clumps denote van der Waals interactions and blue clumps denote hydrogen bonds; (c) Energy-level diagram and frontier-orbital plots for the $\{Ln_2Mo^{IV}_6Mo^{IV}_6P_9\}$ cluster series. (d) Electronic band structure and partial density of states (PDOS) of **6-Eu**. (e) Schematic representation of the k-point path in the Brillouin-zone used for **6-Eu** at the GGA level of theory. (f) Density of states (DOS) of the tetragonal **11-Tb**.

The HOMO-LUMO gaps of Ln_2POMo^{IV}s play a significant role in electronic conductivity performances, in agreement with the fact that cluster pillars markedly contribute to the ETp pathways along *c*-axis. To gain a deeper understanding of the electronic structures and bonding patterns, we performed the first-principles density functional theory (DFT) calculations on $[Ln_2Mo^{IV}_6Mo^{VI}_6(PO_4)_2(HPO_3)_7O_{26}py_6]^{6-}$ at the SDD/def2-TZVP/6-311G* level of theory. The SMD implicit solvation model was employed to account for charge compensation in the calculations of the polyanion clusters. Both the C_{3h}-symmetric **6-Eu** ($4f^6$) and C_s-symmetric **9-Eu** ($4f^6$) clusters exhibit the lowest LUMO energy levels dominated by vacant 4f orbitals and hence the smallest band gaps (**6**, 2.09 eV; **9**, 1.51 eV). The electronic structures benefit for Eu^{III} to receive HOMO electrons to achieve the stable $4f^7$ electron configurations, and to serve as a Eu^{III}⇌Eu^{II} redox pair to promote ETp[36], which account for their good conductive performance.

Density of electronic states (DOS) and band structures based on periodic DFT calculations were performed on the $\{Ln_2(Mo^{IV}_3py_3)_2\}$ clusters. The E_F of **6-Eu** is located on the VBM side, indicative of a *p*-type semiconductor (Fig. 4d). The indirect band gap (E_g) is calculated as 0.86 eV. The sharp peak in DOS across E_F of **11-Tb** indicates that the quasi-aromatic $\{Mo^{IV}_3$-$py_3\}$ SBUs increase the concentration of charge carriers for charge transport that reduced the band gap (Fig. 4f)[37,38]. Both the VBM and CBM for **6-Eu** and **11-Tb** are mainly originated from O, C, N and Mo^{IV} from partial DOS calculations, suggesting that $\{Mo^{IV}_3O_4py_3\}$ units contribute to the narrow bandgap. Thus, the ETp route is conformed to be *d*-π-π-*d* in the Mo^{IV}_3 conjugating layer (Fig. 4d, 4f and S9). We also note that the Fermi level of **6-Eu** lies inside a bandgap, suggesting semiconductive behavior with uniform antiparallel-sandwich π-stacking. In contrast, tetragonal **11-Tb** should exhibit metallic behavior in *ab* plane constructed by triangularly metal–metal bonded Mo^{IV}_3 and comprehensive π-interactions, as evidenced by the bands crossing the Fermi level (Fig. 10)[39]. This metallic-like transport behavior can be bioinspired by the proposition that the electrically conductive pili constructed through comprehensive π-stacking interactions, possess metallic-like conductivity, enabling long-range extracellular electron transfer in microbial systems[34]. The tetragonal systems are of more compact packing (Fig. 1c, 1g and S9) that contributed to higher electrical conductivity.

Remarkably, the hexagonal packing displays ultra-flat bands along the whole Brillouin zone with the valence-band maximum (VBM) bandwidth of merely 0.8 meV and conductance-band maximum (CBM)

bandwidth of 47.8 meV. The ultra-flat band is 246 meV below E_F, which lies very near for *p*-type semiconductors[40]. Kagome lattice has been reported to be a dominant topological structure in inorganic flat band materials except for mott insulators related to exotic physical properties[41-43]. The ultra-flat bands across the entire reciprocal space, in accordance with the isotropic ETp property of single-crystal conductivities for **6-Eu**. Such ultra-flat bands at E_F found in cluster-based crystalline materials for the first time, may add more exotic physical properties that remain uncovered[44].

Conclusion

This study constructs a novel electron-rich molecular crystalline conductor by embedding rare-earth ions into an aromatic $\{Mo^{IV}_3\text{-}py_3\}$ cluster framework. The rare-earth ions guide the formation of extended *d*-π···π-*d* conjugation pathways, effectively overcoming the intrinsic low conductivity of isolated cluster systems. Remarkably, the choice of rare-earth ion induces distinct electronic phases—semiconducting (hexagonal) and metal-like (tetragonal)—while enabling anisotropic conductivity tuning in single crystals. This work not only provides a synthetic strategy for rationally constructing extended conjugated conductive networks in molecular crystals but also showcases the ability to precisely regulate the electronic structure. It offers a clear material design approach and a feasible synthetic pathway for the future on-demand design of molecular functional crystals with tailored conductive, semiconducting, or even metal-like behaviors.

Methods

Synthesis of trinuclear $\{Mo^{IV}_3O_2\}$ cluster precursors

$[Mo_3O_2(O_2CMe)_6(H_2O)_3]ZnCl_4{\cdot}8H_2O$ as the precursor was prepared according to the procedure in previous work.[45,46] A mixture of $Na_2MoO_4{\cdot}H_2O$ (15.0 g), zinc powder (7.5 g), and acetic anhydride (250 mL) was placed in a 500 mL round-bottom flask and heated at 138 °C under reflux with stirring for 48 h. After the reaction was complete, the mixture turned entirely red and was allowed to cool to room temperature, during which a significant amount of red solid formed. The red solid was collected by filtration, and dissolved in 400 mL of hydrochloric acid solution (~1.0 mol L^{-1}; prepared from concentrated HCl/H_2O, 1:10 v/v). The resulting solution was filtered again, and the clear filtrate was left to evaporate slowly in air, yielding red block-shaped crystals.

Synthesis of hexagonal-phase $\{Ln_2(Mo^{IV}_3py_3)_2\}$ cluster crystals

The Mo^{IV} precursor $[Mo_3O_2(O_2CMe)_6(H_2O)_3]ZnCl_4{\cdot}8H_2O$ (0.11 g, 0.1 mmol) and $LaCl_3$ (5.9 mg, 0.024 mmol) and 80% H_3PO_3 solution (52 μL, 0.43 mmol) were added in a 20 mL Teflon-lined autoclave containing 4.8 mL of pyridine, 1.2 mL of water, which were sealed in a stainless-steel and heated under autogenous pressure to 120 °C for 12 h. Then, the mixture was cooled to room temperature at a rate of 1.4 K h^{-1} that produced dark red hexagonal crystals **1-La**. (>30% yield based on Mo). The preparation

process other hexagonal-phase $\{Ln_2(Mo^{IV}{}_3py_3)_2\}$ clusters is similar to that of **1-La**, except that $LaCl_3$ was replaced by their corresponding lanthanide chlorides for **2-Ce** through **7-Gd**.

Synthesis of tetragonal-phase $\{Ln_2(Mo^{IV}{}_3py_3)_2\}$ cluster crystals

The Mo^{IV} precursor $[Mo_3O_2(O_2CMe)_6(H_2O)_3]ZnCl_4{\cdot}8H_2O$ ((0.128 g, 0.13 mmol), $TbCl_3{\cdot}6H_2O$ (10.3 mg, 0.028 mmol) and 80% H_3PO_3 solution (69 μL, 0.57 mmol) were added in a 20 mL Teflon-lined autoclave containing 6 mL of pyridine, 2 mL of water, added in a 20 mL Teflon-lined autoclave containing 4.9 mL of pyridine, 1.1 mL of water, which were sealed in a stainless-steel and heated under autogenous pressure to 115 °C for 12 h. Then, the mixture was cooled to room temperature at a rate of 1.4 K h^{-1} that produced small dark red square crystals. Crimson square crystals of **11-Tb** were harvested (<10% yield based on Mo). The preparation of the other tetragonal $\{Ln_2(Mo^{IV}{}_3py_3)_2\}$ crystals was carried out using a procedure similar to that for **11-Tb**; however, the differences were not limited to the substitution of $TbCl_3{\cdot}6H_2O$ with the corresponding lanthanide chlorides. To drive the reaction to completion and facilitate the hexagonal-to-tetragonal phase transition, the temperature was raised to 120 °C for the Sm, Eu, and Gd analogues. Meanwhile, the H_2O/pyridine solvent ratio was adjusted from 2:8 for **11-Tb** to 2.3:7.7 for **10-Gd**, 2.4:7.6 for **9-Eu**, and 2.6:7.4 for **8-Sm**, respectively. The duration of the constant-temperature step increased progressively for **10-Gd** (19 h), **9-Eu** (22 h), and **8-Sm** (23 h) to accomplish their respective phase transitions, consistent with the effects of lanthanide contraction.

X-ray Crystallography

The X-ray single crystal data for **1-La** and **5**–**11** were collected on an XtaLAB Synergy-R single-crystal diffractometer (RIGAKU Oxford Diffraction) at 100 K, while **2**–**4** were collected on a BRÜKER D8 Venture single-crystal diffractometer using MoKα radiation. All structures were solved by intrinsic phasing method using SHELXT.[47] All non-hydrogen atoms were refined anisotropically using weighted full-matrix least-squares on F^2, and refinements were carried out using SHELXL-2019/3[48] within the graphical interface Olex2-1.5[49]. CCDC-2307759 (**1-La**), CCDC-2307760 (**2-Ce**), CCDC-2307761 (**3-Pr**), CCDC-2307762 (**4-Nd**), CCDC-2307763 (**5-Sm**), CCDC-2307764 (**6-Eu**), CCDC-2307765 (**7-Gd**), CCDC-2307766 (**8-Sm**), CCDC-2307767 (**9-Eu**), CCDC-2307768 (**10-Gd**), CCDC-2307769 (**11-Tb**), contain the supplementary crystallographic data for this paper.

Electronic Property Measurements

Pressed pellets of POM samples were prepared by loading powders into a pressing die with an inner diameter of 3×3 mm and applying a pressure of approximately 400 MPa using a hydraulic pump for 15 min. Both the temperature-dependent electrical conductivity in the range of 250~315 K and Hall effect measurement at ambient temperature were performed by a physical property measurement system (PPMS) based on van der Pauw method with pellet samples. For grown single crystals, DC electrical conductivity was measured in air using two-probe technique. A stabilized DC power supply was used to supply current, and the electrical resistance (*R*) of the samples was measured with a high-impedance

electrometer (Keithley, 6517B). The dimensions of grown single crystals were determined after the measurement using a stereo-microscope (Nikon SM2800). Linear *I–V* curves were obtained by supplying the current and measuring the corresponding voltage. The DC conductivity (σ) was calculated using the well-known relation $\sigma = d/RA$, where d is the thickness of sample and A is the cross-sectional area.

DFT calculations

DFT calculations on single molecular HOMO and LUMO were performed using the GAUSSIAN 16 program package[50] and crystal structure parameters. DFT calculations were carried out using the PBE1PBE functional[51,52]. We have used the Stuttgart/Dresden (SDD) basis set with effective core potentials on Ln atoms[53], def2-TZVP basis set[54] on Mo and 6-311G* basis set[55] on other atoms for the calculations. In these calculations, the solvent effects were taken into account by the solvation model density (SMD)[56]. The natural atomic orbital (NAO) analysis were calculated by the NBO 3.1 module embedded in Gaussian 16 program[50]. The analysis of frontier molecular orbitals and spin densities were performed by Multiwfn 3.8[57-60], which is a multifunctional wavefunction analysis program. The LOL (localized orbital locator) - π delocalization analysis for **1**–**11** were performed using Multiwfn 3.8 package. And the independent gradient model (IGM) analysis were presented using the Multiwfn and VMD packages. For density of state (DOS) and band structure were calculated by performed using the projected augmented wave (PAW) method[61] as implemented in the Vienna Ab Initio Simulation Package (VASP) 6.3.0[62]. The Perdew–Burke–Ernzerhof form of the generalized gradient approximation (PBEGGA) was employed as the exchange-correlation functional[63]. The cutoff energy for plane-wave expansion was taken as 490 eV. The convergence criteria for total energy was 10^{-5} eV. The *k*-point sampling of Brillouin zone was performed by using Monkhorst-Pack grids of 4 × 2 × 4 for hexagonal structures and 2 × 2 × 2 for tetragonal structures, respectively[65]. The vdW correction was incorporated with PBE-D3 method for the non-valent interactions.[65]

Data availability

The crystallographic data reported in this paper are tabulated in the supplementary materials and archived at the Cambridge Crystallographic Data Centre under reference numbers CCDC 2307759–2307769 (**1-La** to **11-Tb**). All other relevant data supporting the findings of this study are presented in the paper or the supplementary materials.

Declarations

Acknowledgments

We acknowledge the support from the National Natural Science Foundation of China (Grant No. 21873102, 22371278, U23A2095 and 22478119) and the Funding of Fujian Provincial Chemistry Discipline Alliance (50025401).

Author contributions

L.X. and W.F. provided experimental, theoretical guidance and supervised the work. Z.L. carried out the experiments, analyzed data and performed the density functional theory calculations. S.L. and C.R. carried out the experiments. Q.F., Z.L. and C.L. performed the electronic conduction measurements. Z.L., L.X., W.F. and M.L. discussed the results and commented on the manuscript. L.X., W.F. and L.Z. provided experimental resources. Z.L. and L.X. wrote the manuscript. W.F. revised the manuscript for submission.

Competing interests

The authors declare no competing interests.

References

1. Batail, P. Introduction: Molecular Conductors. *Rev.***104**, 4887–4890 (2004).
2. Coronado, E. & Galán-Mascarós, J. R. Hybrid molecular conductors. *Mater. Chem.***15**, 66–74 (2005).
3. Jeong, H. *et al.* Uninterrupted *π-d* Conjugated Three-Dimensional Conductive Metal–Organic Framework. *ACS Mater. Lett.***7**, 2056–2062 (2025).
4. Bian, G., Yin, J. & Zhu, J. Recent advances on conductive 2D covalent organic frameworks. *Small***17**, 2006043 (2021).
5. Schubert, U. Cluster-based inorganic–organic hybrid materials. *Soc. Rev.***40**, 575–582 (2011).
6. Zhang, J., Feng, P., Bu, X. & Wu, T. Atomically precise metal chalcogenide supertetrahedral clusters: frameworks to molecules, and structure to function. *Sci. Rev.***9**, nwab076 (2022).
7. Gumerova, N. I. & Rompel, A. Synthesis, structures and applications of electron-rich polyoxometalates. *Rev. Chem.***2**, 0112 (2018).
8. Kondinski, A. Metal–metal bonds in polyoxometalate chemistry. *Nanoscale***13**, 13574–13592 (2021).
9. Horn, M. R. *et al.* Polyoxometalates (POMs): from electroactive clusters to energy materials. *Energy Environ. Sci.***14**, 1652–1700 (2021).
10. Long, D.-L., Burkholder, E. & Cronin, L. Polyoxometalate clusters, nanostructures and materials: From self assembly to designer materials and *Chem. Soc. Rev.***36**, 105–121 (2007).
11. Chu, J. *et al.* Electronic band structure engineering of *π-d* conjugated metal-organic framework for sodium organic batteries. *Commun.***16**, 3549 (2025).
12. Coronado, E., Giménez-Saiz, C. & Gómez-García, C. J. Recent advances in polyoxometalate-containing molecular conductors. *Chem. Rev.***249**, 1776–1796 (2005).
13. Sun, L., Campbell, M. G. & Dincă, M. Electrically conductive porous metal–organic frameworks. *Chem. Int. Ed.***55**, 3566–3579 (2016).
14. Coronado, E. & Gómez-García, C. J. Polyoxometalate-based molecular materials. Chem. Rev. 98, 273–296 (1998).
15. Kuc, A. Low-dimensional transition-metal dichalcogenides. (2014).

16. Bellitto, C., Bauer, E. M. & Righini, G. Organic–inorganic hybrids: from magnetic perovskite metal (II) halides to multifunctional metal (II) phosphonates. *Chem. Rev.***289**, 123–136 (2015).
17. Zheng, C.-S. Tsang, L. Y. S. Lee, K.-Y. Wong, Two-dimensional metal-organic framework and covalent-organic framework: synthesis and their energy-related applications. *Mater. Today Chem.***12**, 34–60 (2019).
18. Wang, F. Gao, Z. Kang, W. Fan, D. Sun, Reticular chemistry within three-dimensional covalent organic frameworks for multiple applications. *J. Mater. Chem. A***11**, 20368–20382 (2023).
19. Xu, B.-L. Luo, L.-L. Wang, L. Xu, An unprecedented nanocage-like and heterometallic [$Mo^{IV}_3O_4$]-polyoxomolybdate hybrid. *Dalton Trans.***47**, 3218–3222 (2018).
20. Wang, B. & Li, W.-L. Revisiting the quasi-aromaticity in polynuclear metal chalcogenide clusters and their derivative “cluster-assembly” crystalline structures. *Chem. Chem. Phys.***26**, 17370–17382 (2024).
21. Li, J., Liu, C.-W. & Lu, J.-X. Electronic structures and *d-pπ* bonding of some $M_3X_4^{4+}$ cluster compounds. *Polyhedron***13**, 1841–1851 (1994).
22. Zhu, Y. *et al.* Silver-Templated γ-Keggin Alkyltin-Oxo Cluster: Electronic Structure and Optical Limiting Effect. *Chem. Int. Ed.***61**, e202202853 (2022).
23. Partyka, D. V., Staples, R. J. & Holm, R. Nucleophilic reactivity and oxo/sulfido substitution reactions of $M^{VI}O_3$ Groups (M= Mo, W). *Chem.***42**, 7877–7886 (2003).
24. Ren, C. *et al.* Deeply reduced empty Keggin clusters [$Mo^{IV}_xM^{VI}_{12-x}O_{40-x}py_x$] (x= 3, 6; M= Mo, W; py= pyridine): synthesis, structures, and Lewis field catalysis. *Chem. Front.***8**, 5178–5185 (2021).
25. Lin, S., Lu, Z. & Xu, L. Hollow Keggin-Type Hybrid Polyoxometalate as a Stable Redox Electrode for Safe and Fast-Charging Lithium-Ion Batteries. *Growth Des.***25**, 10134–10142 (2025).
26. K. Sahu *et al.*, Microwave synthesis of molybdenene from MoS_2. *Nat. Nanotechnol.***18**, 1430–1438 (2023).
27. E. González-Rosende, E. Castillo, W. B. Jennings, J. F. Malone, Stereodynamics and edge-to-face CH–π aromatic interactions in imino compounds containing heterocyclic rings. *Org. Biomol. Chem.***15**, 1484–1494 (2017).
28. Tsunashima *et al.*, Electrical network of single-crystalline metal oxide nanoclusters wired by π-molecules. *Angew. Chem. Int. Ed.***126**, 11410–11413 (2014).
29. Xie, L. S., Skorupskii, G. & Dincă, M. Electrically conductive metal–organic frameworks. *Rev.***120**, 8536–8580 (2020).
30. Skorupskii, G. & Dincă, M. Electrical conductivity in a porous, cubic rare-earth catecholate. *Am. Chem. Soc.***142**, 6920–6924 (2020).
31. L. Chen *et al.*, Conductive Lanthanide Metal–Organic Frameworks with Exceptionally High Stability. *J. Am. Chem. Soc.***145**, 16983–16987 (2023).

32. Xie, L. S. *et al.* Tunable mixed-valence doping toward record electrical conductivity in a three-dimensional metal–organic framework. *Am. Chem. Soc.***140**, 7411–7414 (2018).
33. E. Yalcin *et al.*, Electric field stimulates production of highly conductive microbial OmcZ nanowires. *Nat. Chem. Biol.***16**, 1136–1142 (2020).
34. J. Dahl *et al.*, A 300-fold conductivity increase in microbial cytochrome nanowires due to temperature-induced restructuring of hydrogen bonding networks. *Sci. Adv.***8**, eabm7193 (2022).
35. Lefebvre *et al.*, The independent gradient model: a new approach for probing strong and weak interactions in molecules from wave function calculations. *ChemPhysChem***19**, 724–735 (2018).
36. Wang *et al.*, A Eu^{3+}-Eu^{2+} ion redox shuttle imparts operational durability to Pb-I perovskite solar cells. *Science***363**, 265–270 (2019).
37. Duan *et al.*, Cataloging High-Quality Two-Dimensional van der Waals Materials with Flat Bands. *Adv. Funct. Mater.*, 2313067 (2024).
38. Kröger *et al.*, P-type doping of organic wide band gap materials by transition metal oxides: A case-study on molybdenum trioxide. *Org. Electron.***10**, 932–938 (2009).
39. Skorupskii *et al.*, Efficient and tunable one-dimensional charge transport in layered lanthanide metal–organic frameworks. *Nat. Chem.***12**, 131–136 (2020).
40. X. Shen, D. S. Dessau, Electronic structure and photoemission studies of late transition-metal oxides —Mott insulators and high-temperature superconductors. *Phys. Rep.***253**, 1–162 (1995).
41. Regnault, N. et al. Catalogue of flat-band stoichiometric materials. *Nature***603**, 824-828 (2022).
42. Yin, J.-X., Lian, B. & Hasan, M.Z. Topological kagome magnets and superconductors. *Nature***612**, 647-657 (2022).
43. Jiang, W., Ni, X. & Liu, F. Exotic topological bands and quantum states in metal–organic and covalent–organic frameworks. *Chem. Res.***54**, 416–426 (2021).
44. Heine, M. Dincă, G. Zhu. Physical Phenomena in Porous Frameworks *Acc. Chem. Res.*, **58**, 327–329 (2025).
45. Luo, B.; Xu, L. POM-FLPs: $[Mo^{IV}_3]_n$-polyoxometalate bifunctional catalysis by $[Mo^{IV}_3]_n$–O_m Lewis pairs frustrated by triangular Mo^{IV}–Mo^{IV} bonds. *Dalton Trans.* **2019**, *48* (20), 6892-6898.
46. Bino, A., Cotton, F. A. & Dori, Z. A trinuclear molybdenum (IV) cluster compound having an unusual structure and unusual stability. *J. Am. Chem. Soc.* **100**, 5252–5253 (1978).
47. Sheldrick, G. M. SHELXT–Integrated space-group and crystal-structure determination. *Acta Crystallographica Section A: Foundations and Advances* **71**, 3–8 (2015).
48. Sheldrick, G. M. Crystal structure refinement with SHELXL. *Acta Crystallogr. C* **2015**, *71* (1), 3-8.
49. Dolomanov, O. V.; Bourhis, L. J.; Gildea, R. J.; Howard, J. A.; Puschmann, H. OLEX2: a complete structure solution, refinement and analysis program. *J. Appl. Crystallogr.* **2009**, *42* (2), 339-341.
50. Gaussian 16, Revision C.01, M. J. Frisch, G. W. Trucks, H. B. Schlegel, G. E. Scuseria, M. A. Robb, J. R. Cheeseman, G. Scalmani, V. Barone, G. A. Petersson, H. Nakatsuji, X. Li, M. Caricato, A. V.

Marenich, J. Bloino, B. G. Janesko, R. Gomperts, B. Mennucci, H. P. Hratchian, J. V. Ortiz, A. F. Izmaylov, J. L. Sonnenberg, D. Williams-Young, F. Ding, F. Lipparini, F. Egidi, J. Goings, B. Peng, A. Petrone, T. Henderson, D. Ranasinghe, V. G. Zakrzewski, J. Gao, N. Rega, G. Zheng, W. Liang, M. Hada, M. Ehara, K. Toyota, R. Fukuda, J. Hasegawa, M. Ishida, T. Nakajima, Y. Honda, O. Kitao, H. Nakai, T. Vreven, K. Throssell, J. A. Montgomery, Jr., J. E. Peralta, F. Ogliaro, M. J. Bearpark, J. J. Heyd, E. N. Brothers, K. N. Kudin, V. N. Staroverov, T. A. Keith, R. Kobayashi, J. Normand, K. Raghavachari, A. P. Rendell, J. C. Burant, S. S. Iyengar, J. Tomasi, M. Cossi, J. M. Millam, M. Klene, C. Adamo, R. Cammi, J. W. Ochterski, R. L. Martin, K. Morokuma, O. Farkas, J. B. Foresman and D. J. Fox. Gaussian~16 rEvision c.01, 2016, Gaussian Inc. Wallingford CT.

51. Perdew, J. P.; Burke, K.; Ernzerhof, M. Generalized gradient approximation made simple. Phys. Rev. Lett. 1996, 77 (18), 3865.
52. Adamo, C.; Barone, V. Toward reliable density functional methods without adjustable parameters: The PBE0 model. *J. Chem. Phys.* **1999**, *110* (13), 6158-6170.
53. Weigend, F.; Ahlrichs, R. Balanced basis sets of split valence, triple zeta valence and quadruple zeta valence quality for H to Rn: Design and assessment of accuracy. *Phys. Chem. Chem. Phys.* **2005**, *7* (18), 3297-3305.
54. Dolg, M.; Wedig, U.; Stoll, H.; Preuss, H. Energy-adjusted ab initio pseudopotentials for the first row transition elements. *J. Chem. Phys.* **1987**, *86* (2), 866-872.
55. Stephens, P. J.; Devlin, F. J.; Chabalowski, C. F.; Frisch, M. J. Ab initio calculation of vibrational absorption and circular dichroism spectra using density functional force fields. *J. Phys. Chem.* **1994**, *98* (45), 11623-11627.
56. Marenich, A. V.; Cramer, C. J.; Truhlar, D. G. Universal solvation model based on solute electron density and on a continuum model of the solvent defined by the bulk dielectric constant and atomic surface tensions. *J. Phys. Chem. B* **2009**, *113* (18), 6378-6396.
57. Lu, T.; Chen, F. Multiwfn: A multifunctional wavefunction analyzer. *J. Comput. Chem.* **2012**, *33* (5), 580-592.
58. Lu, T.; Chen, Q. A simple method of identifying π orbitals for non-planar systems and a protocol of studying π electronic structure. *Theor. Chem. Acc.* **2020**, *139* (2), 25.
59. Lefebvre, C.; Rubez, G.; Khartabil, H.; Boisson, J.-C.; Contreras-García, J.; Hénon, E. Accurately extracting the signature of intermolecular interactions present in the NCI plot of the reduced density gradient versus electron density. *Phys. Chem. Chem. Phys.* **2017**, *19* (27), 17928-17936.
60. Lu, T.; Chen, Q. Independent gradient model based on Hirshfeld partition: A new method for visual study of interactions in chemical systems. *J. Comput. Chem.* **2022**, *43* (8), 539-555.
61. Kresse, G.; Furthmüller, J. Efficient iterative schemes for ab initio total-energy calculations using a plane-wave basis set. *Phys. Rev. B* **1996**, *54* (16), 11169.
62. Blöchl, P. E. Projector augmented-wave method. *Phys. Rev. B* **1994**, *50* (24), 17953.
63. Perdew, J. P.; Burke, K.; Ernzerhof, M. Generalized gradient approximation made simple. *Phys. Rev. Lett.* **1996**, *77* (18), 3865.

64. Monkhorst, H. J.; Pack, J. D. Special points for Brillouin-zone integrations. *Phys. Rev. B* **1976**, *13* (12), 5188.
65. Grimme, S.; Antony, J.; Ehrlich, S.; Krieg, H. A consistent and accurate ab initio parametrization of density functional dispersion correction (DFT-D) for the 94 elements H-Pu. *J. Chem. Phys.* **2010**, *132* (15).

Scheme

Scheme 1 and 2 is available in the Supplementary Files section.

Figures

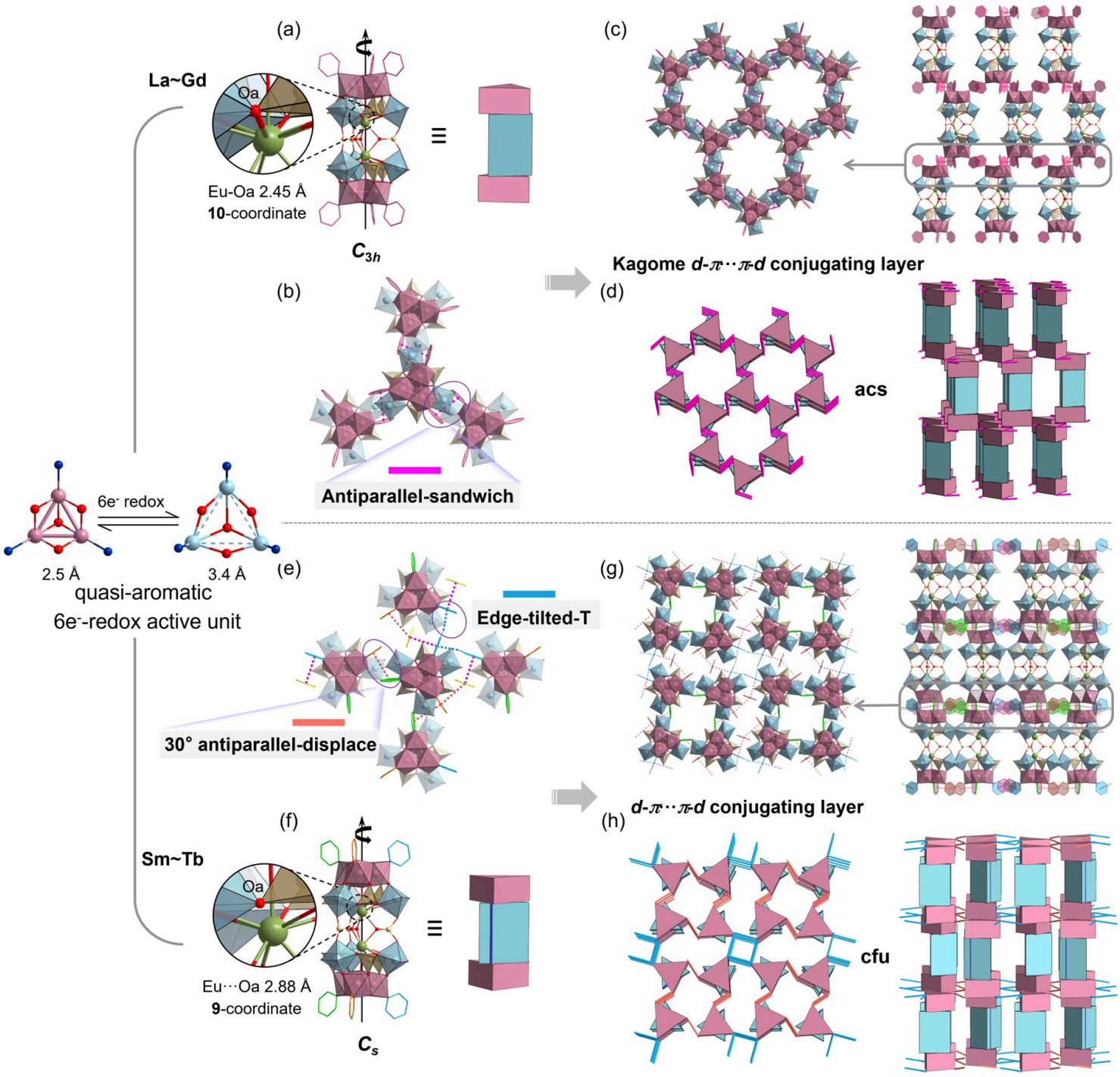


Figure 1

Assembly of *d*-π···π-*d* conductive networks in molecular-cluster crystals, directed by lanthanide ions, modulated by their coordination environment (geometry, coordination number, and symmetry). (a, f) Coordination environments of the lanthanide ion in the hexagonal phase (10-coordinate, C_{3h} symmetry) and the tetragonal phase (9-coordinate, C_s symmetry), respectively, with Eu–O_a bond lengths labeled (2.45 Å in the hexagonal phase and 2.28 Å in the tetragonal phase). Color shading highlights the structural features of the lanthanide coordination units. (b) Primary structural building units of the hexagonal-phase clusters assembled in an antiparallel-sandwich arrangement. (c) Further assembly into

Kagome-type *d*-*π*···*π*-*d* conjugated layers in the hexagonal phase. (d) 3D crystalline network with **acs** topology constructed from the hexagonal phase. (e) Assembly features of the quasi-aromatic $\{Mo^{IV}_3O_4\}$ cluster units in the tetragonal phase, exhibiting a 30° antiparallel displaced and edge-tilted-T *π*···*π* stacking configuration. (g) *d*-*π*···*π*-*d* conjugated layer structure formed in the tetragonal phase. (h) Finally, 3D crystalline network with **cfu** topology constructed from the tetragonal phase. Color code: Mo^{IV}, red purple; Mo^{VI}, teal; Ln, olive; P, pale brown; O, red; C, gray; antiparallel-sandwich stacked py, magenta; edge-tilted-T stacked py, sky blue; mono 30° antiparallel-displaced py, light green; dual 30° antiparallel-displaced py, orange; lattice py, yellow. H atoms are omitted for clarity.

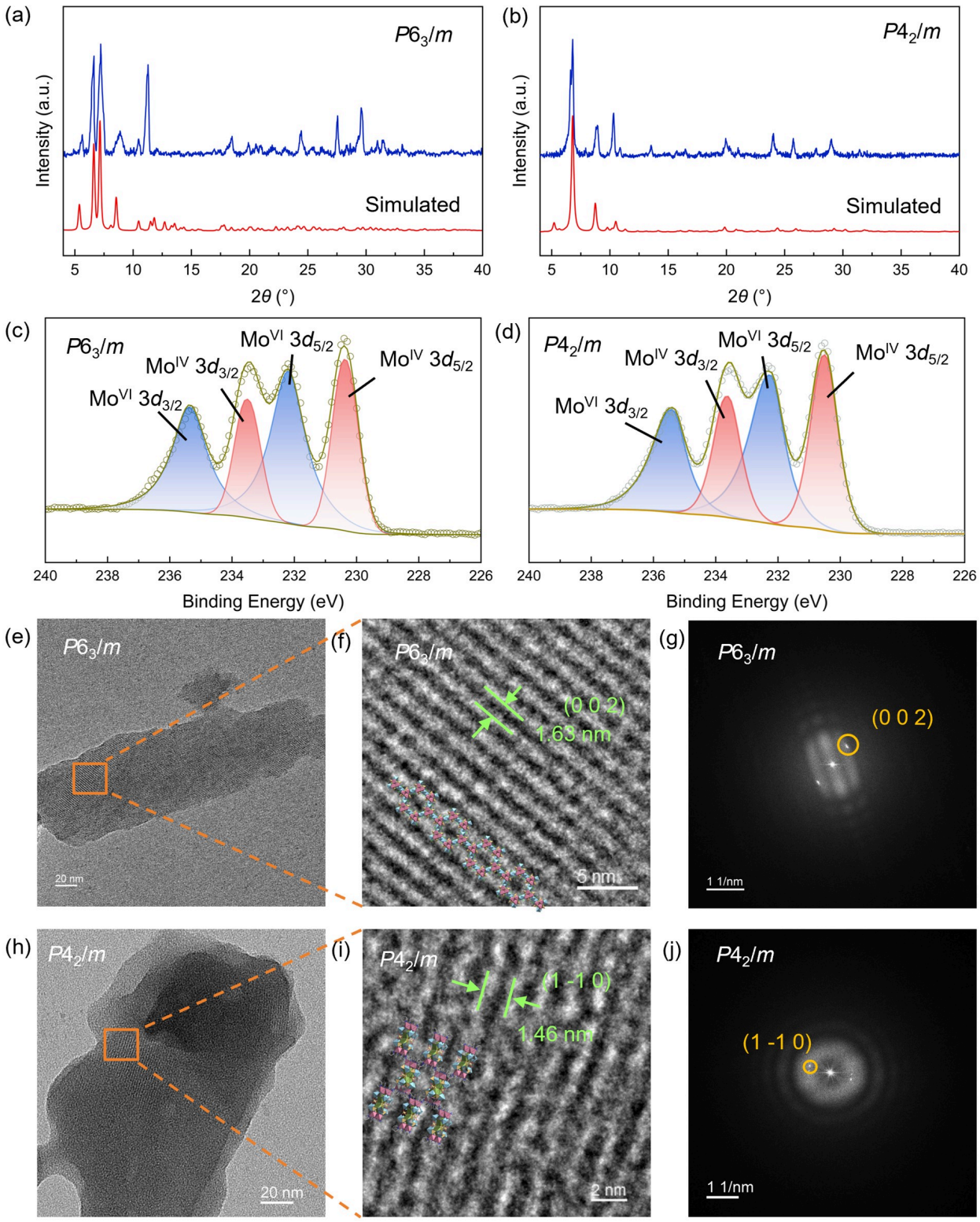


Figure 2

Structural characterization of $\{Ln_2(Mo^{IV}_3py_3)_2\}$ clusters through XRD, XPS, and electron microscopy. (a, b) Experimental and simulated powder X-ray diffraction (PXRD) patterns for $\{Ln_2(Mo^{IV}_3py)_2\}$ clusters in the hexagonal (a) and tetragonal (b) phases, demonstrating phase purity and structural agreement. (c, d) XPS analysis confirming the Mo^{IV} state. (e–j) Field emission transmission electron microscopy (FETEM)

images and FFT patterns displaying the crystallinity and lattice structure of the hexagonal (e-g) and tetragonal (h-j) phases.

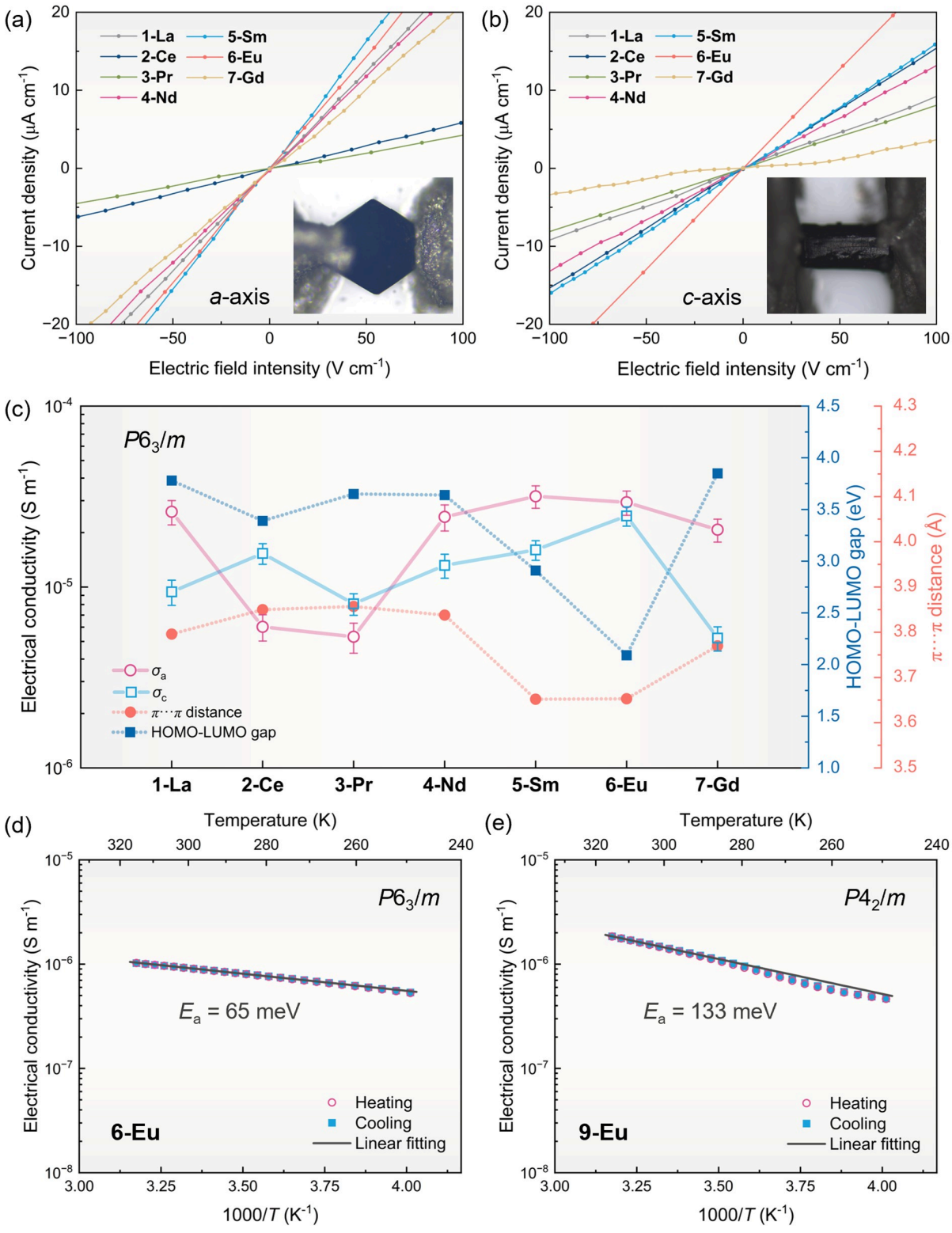


Figure 3

Electrical conductivity characterization of $\{Ln_2(Mo^{IV}_3py_3)_2\}$ materials: (a) Typical *I*–*V* curves showing the single-crystal conductivity of $P6_3/m$ symmetric **1–7** along the *a*-axis, acquired using the two-probe

method. (b) Typical *I*–*V* curves showing their conductivity along the *c*-axis. (c) Summary of single-crystal conductivity (*a*- and *c*-axis), HOMO–LUMO gaps, and π-stacking distance of the aromatic clusters. (d, e) Arrhenius representation of the pellet electrical conductivity for hexagonal **6-Eu** (d) and tetragonal **9-Eu** (e), measured via the van der Pauw method.

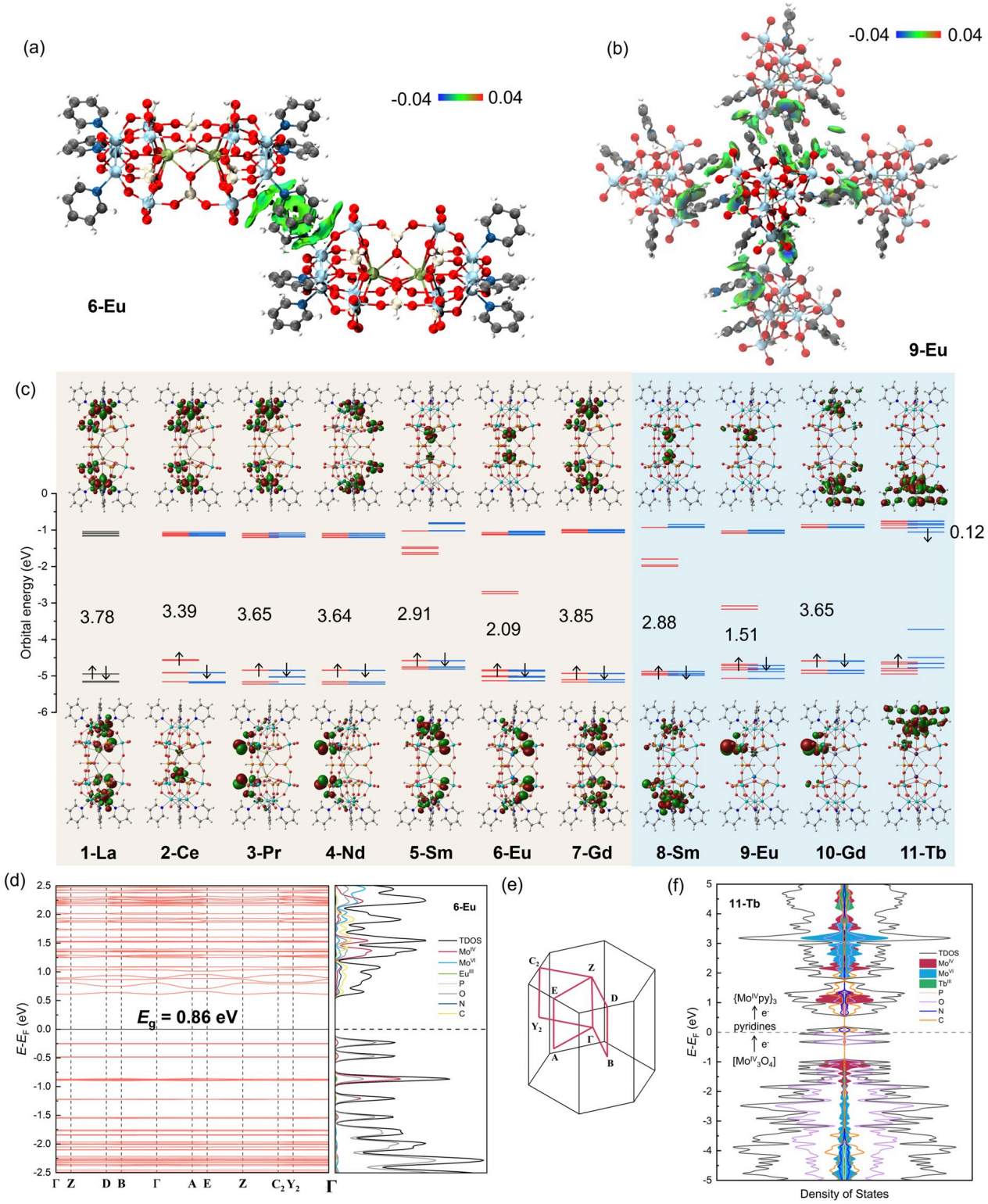


Figure 4

Colored isosurfaces (isosurface value = 0.006) showing IGM (independent-gradient-model) analysis of multiple Mo^{IV}–π conjugations: (a) the dimer of **6-Eu** under hexagonal symmetry, and (b) the pentamer of **9-Eu** under tetragonal symmetry, in which green clumps denote van der Waals interactions and blue clumps denote hydrogen bonds; (c) Energy-level diagram and frontier-orbital plots for the $\{Ln_2Mo^{IV}_6Mo^{IV}_6P_9\}$ cluster series. (d) Electronic band structure and partial density of states (PDOS) of **6-Eu**. (e) Schematic representation of the k-point path in the Brillouin-zone used for **6-Eu** at the GGA level of theory. (f) Density of states (DOS) of the tetragonal **11-Tb**.

Supplementary Files

This is a list of supplementary files associated with this preprint. Click to download.

- 5Sm.cif
- 3Pr.cif
- 6Eu.cif
- 7Gd.cif
- 11Tb.cif
- 8Sm.cif
- 2Ce.cif
- 10Gd.cif
- 1La.cif
- 4Nd.cif
- 9Eu.cif
- SupplementaryMaterials1.21.docx
- XLn2MoIV3py32XCIFs.cif
- SupplementaryVideos.zip
- Scheme1.jpg
- Scheme2.jpg